Endoproteolysis of Oligopeptide-Based Coacervates for Enzymatic Modeling

Zhicheng Jin◆,

Department of NanoEngineering, University of California, San Diego, La Jolla 92093 California, United States

Chuxuan Ling◆,

Department of NanoEngineering, University of California, San Diego, La Jolla 92093 California, United States

Wonjun Yim,

Materials Science and Engineering Program, University of California, San Diego, La Jolla 92093 California, United States

Yu-Ci Chang,

Materials Science and Engineering Program, University of California, San Diego, La Jolla 92093 California, United States

Tengyu He,

Materials Science and Engineering Program, University of California, San Diego, La Jolla 92093 California, United States

Ke Li,

Institute of Materials Research and Engineering (IMRE), Agency for Science, Technology and Research (A*STAR), Singapore 138634, Republic of Singapore

Jiajing Zhou,

Department of NanoEngineering, University of California, San Diego, La Jolla 92093 California, United States

Yong Cheng,

Department of NanoEngineering, University of California, San Diego, La Jolla 92093 California, United States

Yi Li,

Department of NanoEngineering, University of California, San Diego, La Jolla 92093 California, United States

Corresponding Author Jesse V. Jokerst – Department of NanoEngineering, Materials Science and Engineering Program, and Department of Radiology, University of California, San Diego, La Jolla 92093 California, United States; jjokerst@ucsd.edu.
◆Author Contributions

Justin Yeung,

Department of Bioengineering, University of California, San Diego, La Jolla 92093 California, United States

Ruijia Wang,

Department of Pediatrics, School of Medicine, University of California, San Diego, La Jolla 92093 California, United States

Pavla Fajtová,

Skaggs School of Pharmacy and Pharmaceutical Sciences, University of California, San Diego, La Jolla 92093 California, United States

Lubna Amer,

Materials Science and Engineering Program, University of California, San Diego, La Jolla 92093 California, United States

Hedi Mattoussi,

Department of Chemistry and Biochemistry, Florida State University, Tallahassee 32306 Florida, United States

Anthony J. O'Donoghue,

Skaggs School of Pharmacy and Pharmaceutical Sciences, University of California, San Diego, La Jolla 92093 California, United States

Jesse V. Jokerst

Department of NanoEngineering, Materials Science and Engineering Program, and Department of Radiology, University of California, San Diego, La Jolla 92093 California, United States

Abstract

Better insights into the fate of membraneless organelles could strengthen the understanding of the transition from prebiotic components to multicellular organisms. Compartmentalized enzyme reactions in a synthetic coacervate have been investigated, yet there remains a gap in understanding the enzyme interactions with coacervate as a substrate hub. Here, we study how the molecularly crowded nature of the coacervate affects the interactions of the embedded substrate with a protease. We design oligopeptide-based coacervates that comprise an anionic Asp-peptide (D_{10}) and a cationic Arg-peptide (R_5R_5) with a proteolytic cleavage site. The coacervates dissolve in the presence of the main protease (M^{pro}) implicated in the coronavirus lifecycle. We capitalize on the condensed structure, introduce a self-quenching mechanism, and model the enzyme kinetics by using Cy5.5-labeled peptides. The determined specificity constant (k_{cat}/K_M) is 5817 M^{-1} s^{-1} and is similar to that of the free substrate. We further show that the enzyme kinetics depend on the type and quantity of dye incorporated into the coacervates. Our work presents a simple design for enzyme-responsive coacervates and provides insights into the interactions between the enzyme and coacervates as a whole.

Graphical Abstract
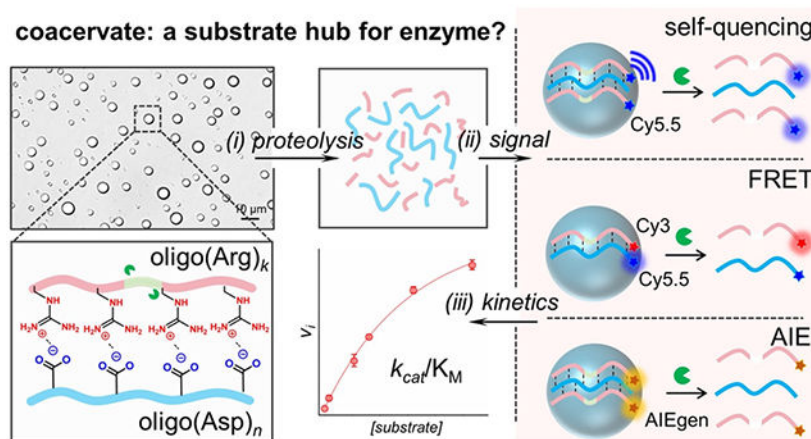
INTRODUCTION

Membraneless organelles within cells are now recognized to exhibit liquid-like properties that arise from the coalescence of functional biomolecules. These include stress granules and processing bodies (P-bodies) that recruit mRNA and RNA-binding proteins through liquid–liquid phase separation (LLPS) or coacervation.[1-4] Investigations into the fate of these organelles, as well as their responsive to stimuli such as pH,[5] redox potential,[6] light,[7,8] and enzymes,[9] among others, could strengthen the understanding of the progression from inanimate prebiotic components to life. Recent studies have shed light on the factors influencing stress granules. Taylor et al. reported that a light-triggered chimeric protein could drive their condensation in cells,[2,7] and Wang et al. highlighted the impact of energy deficiency on the generation and clearance of stress granules through protein complex assembly or RNA condensation.[10] In related studies of P-bodies, these condensed organelles are believed to prevent the constituting mRNA from ribonuclease degradation, yet decay of specific mRNA may still occur in these hubs.[11-13] This indicates the complex and elusive nature of the interplay between nonmembrane organelles and enzymes.

Synthetic coacervates, which mimic membrane-free organelles, have gained significant attention for their ability to uncover the dynamics such as compartmentalization,[8,9,14] mesostructured manipulations,[15-18] and local reactions,[19,20] among others. Proteases are key participants in many biological events in cells, with proteolytic processing being critical to post modification, activity regulation, protein turnover, and signal transduction. *In vitro* evidence from Rosen et al. and Keating et al. have demonstrated that kinase and phosphatase can manipulate the reversible formation of coacervates by modifying the phosphorylation states and Coulombic interactions among the comprising peptides.[9,21] Although effective, this strategy stringently requires a sufficient number of phosphorylatable Ser residues in the substrate. Furthermore, the kinetics of the enzyme on coacervate as a substrate hub remains largely unexplored.

In this article, we present a simple model for studying the endoproteolysis of complex coacervates. The coacervates were designed with oppositely charged peptides that coded a specific cleavage site, e.g., D_{10} and R_5R_5 peptides. We validated the system's response to coronavirus main protease (M^{pro}) *in vitro*. Upon cleavage of the concentrated R_5R_5 substrate, M^{pro} reduced the charge valence and weakened the electrostatic interactions, leading to the disassembly of the coacervates. To quantify the proteolytic kinetics of the coacervates by M^{pro}, we further introduced the Cy5.5-R_5R_5 conjugate to the coacervates as optical reporters. For example, a significant reduction in dye photoluminescence (PL) was realized via a self-quenching (or contact quenching) mechanism upon confinement within the droplets, while the dye PL recovered in the presence of M^{pro}. We found that the molecularly crowded nature of the coacervate had a minimal impact on the catalytic efficiency (k_{cat}/K_M) of the protease on the substrate in the coacervates. In addition, the results from other transduction mechanisms such as fluorescence resonance energy transfer (FRET) and aggregation-induced emission (AIE) revealed that doubling the amount of dye completely halted the protease from interacting with the coacervates. Finally, we confirmed that dye molecules trapped within the coacervates could be fully released with M^{pro} stimulation. Our results provide valuable insights into the interactions between the protease and nonmembrane coacervates and suggest an alternative model for studying enzymes.

RESULTS AND DISCUSSION

Rationale

Modeling the interactions between coacervates and proteases was motivated by the desire to understand how the nonmembrane organelles could respond to enzymatic stimuli. Complex coacervation is an LLPS resulting from the interactions of two or more oppositely charged macroions.[22] Charged amino acid residues are important for regulating protein condensation in cells by forming ion pairs, hydrogen bonds, and nonspecific electrostatic interactions.[23,24]

Our representative coacervates used R_5R_5 and D_{10} peptides (Figure 1a). The modular cationic peptide has two charged $(Arg)_5$ termini flanking a specific M^{pro} cleavage site, and the counterpart uses a decapeptide, $(Asp)_{10}$. The prevalent electrostatic interactions between the two peptides yield complex coacervates because of the charge valence of 10 seen on the backbone from positive guanidine and negative carboxylate groups.[25] M^{pro} is used as a model protease because it processes viral polypeptides into functional proteins and, thus, is important for diagnostics and therapeutics, e.g., Paxlovid.[26] In Figure 1b, we hypothesized that endoproteolysis of the cationic R_5R_5 peptides would halve their charge multivalency, thus weakening Coulombic attractions and dissolving coacervates. Moreover, we employed dye-labeled peptides to construct optically addressable coacervates, which evaluate enzymatic kinetics via transduction mechanisms, such as self-quenching, FRET, and AIE (Figure 1c).

Initial experiments focused on optimizing the peptide sequence (charge valence, net charge) and coacervation conditions (pH, charge ratio, surfactant, *etc*). The coacervates were then characterized by optical absorption, dynamic light scattering (DLS), transmission electron microscopy (TEM), confocal microscopy, mass spectroscopy, and gel electrophoresis. The enzyme kinetic of the coacervates by M^{pro} was quantified. The effects of molecular

crowdedness and hydrophobicity of coacervates on the proteolysis were discussed. We also exploited enzyme assays such as sensitivity, specificity, inhibition, and matrix effects. Finally, we evaluated the coacervate as a potential delivery system triggered by enzyme.

Oligopeptide Coacervates

The effects of charge on complex coacervation were studied, including charge valence, charge density, and net charge. Table 1 summarizes the peptides used in this work. For example, the cationic R_{10} decapeptide was derivatized to an R_kR_l formula (k, l–number of repeating unit) to encompass varying charge valency and a central M^{pro} cleavage sequence, AVLQ↓SGF.[27] In Figure 2a, the mass spectrum of R_5R_5 (i.e., RRRRRAVLQ↓SGFRRRRR) showed a strong peak at 2282.9 that was attributed to its $[M + H]^+$ ion (calcd 2280.4). Incubating R_5R_5 with M^{pro} in phosphate buffer (20 mM, pH 8.0) at 37 °C for 1 h resulted in peaks at 1209.8 and 1088.6, ascribed to the $[M + H]^+$ ion of the N-terminal (calcd 1209.8) and C-terminal fragments (calcd 1088.7), respectively. This indicates successful peptide synthesis and enzyme cleavage. The mass spectra of other substrates also nicely matched the calculated values (Figures S1-S4).

The anionic counterparts used D_{10} and D_5D_5 peptides for coacervation. In addition, zwitterionic peptides were designed and synthesized such as $R_{10}D_5$, $R_{10}D_{10}$, and R_5D_{10}, with varying net charges of +5, 0, and −5, respectively. The opposite charge on the peptide backbones above leads to ion-pairing interactions that drive complex coacervation.

We first evaluated the impact of *charge valence* on the coacervation of R_kR_l ($k+l = 5$, 7, and 10) with D_{10}. Upon mixing these oppositely charged oligopeptides, two outcomes were observed: a clear solution and a coacervate emulsion. The conditions used 5 mM total charge, 0.5 charge ratio, 20 mM phosphate buffer (PB) at pH 8, and 0.2% w/v Tween-20 unless otherwise indicated. In Figure 2b, the minimal charge valence for coacervation was found to be $(k+l)_{min} = 10$ (second column), which also held true for D_5D_5 (first column). For example, the coacervation occurred between combinations of (R_5R_5, D_{10}), (R_{10}, D_{10}), (R_5R_5, D_5D_5), and (R_5R_5, D_{10}), while R_2R_3 and R_3R_4 failed to condense with D_{10} or D_5D_5 (Table 2). This notion agrees with Keating and co-workers' findings that the shortest length of peptidic polyions for coacervation is 10 due to the critical amount of ion-pairing interactions.[25] This also suggests that the inner positioning of the cleavage site in R_kR_l (e.g., at the center for R_5R_5) is essential for the current design. It enables the intact coacervation of R_5R_5 with D_{10}, while predicting the subsequent coacervate disassembly after endoproteolysis. Work from other groups and ours also emphasizes the significance of a polyion's electrophoretic characteristics in dictating the least charge valence of its counterpart required for coacervation:[22,32] we observed coacervation when mixing R_3R_4 with the zwitterionic R_5D_{10} peptide, which can be attributed to the pendant R_5 domain on the zwitterionic backbone reinforcing electrostatic interactions (third column, and Figure S5). These combined observations highlight the commensurate charge valence in the governing complex coacervation.

Subsequently, we probed the impact of the *net charge* of the peptide on the coacervation dynamics. The net charge of −5 carried by the zwitterionic R_5D_{10} peptide exhibited coacervation properties similar to those of D_{10} (see second vs third column, Figure 2b).

Likewise, numerous droplets resulted from mixing the zwitterionic $R_{10}D_5$ with either D_{10} or D_5D_5 peptide. We further report that the zwitterionic $R_{10}D_{10}$ of a zero net charge self-coacervates with the emergence of surface wrinkles on the droplets (Figure S6). Therefore, the effect of the net charge is marginal on the formation of coacervates.

In contrast, the *net charge* has an important implication on the colloidal stability of coacervates.[33] This is indicated by the zeta potential (ζ) and hydrodynamic diameter (D_H) values in Table 2. For example, the combination of ($R_{10}D_5$, D_{10}) yielded the most stable droplets with a low surface potential of -10.4 ± 1.1 mV and a compact size of $D_H = 0.25$ μm (Figure S7). This low potential is due to the negatively charged D_5 moiety on $R_{10}D_5$. In addition, $\zeta_{(R5R5, D10)}$ and $\zeta_{(R10, D5D5)}$ at -6 to -7 mV showed moderate stabilities with larger sizes ($D_H = 0.65$ μm), while the positively charged R_5 moiety in the R_5D_{10} peptide neutralized and reversed the zeta potential and led to unstable and larger droplets when mixing with R_{10} (Figures S5,6). This suggests the importance of tuning the net charge on constituting peptides to enhance colloidal stability and compactness. These findings align with recent studies that highlight the surface electrostatics and viscosity in governing the stability of condensates.[33]

To this end, the role of *charge density* in complex coacervation has been explored, which refers to the charge valence per unit length.[22,34] In the first, despite R_5 and R_{10} having similar charge densities, coacervation was observed only in the (R_{10}, D_{10}) mixture and not with (R_5, D_{10}) under the same conditions (Figure S5). In the second, R_5R_5 peptide coacervated with D_{10} despite being almost twice as long as R_{10} with the same charge valence (third row in Figures 2a and S5). We found similar coacervation abilities of D_{10} and D_5D_5 (first vs second column, Figure 2a). These observations, coupled with the existing literature,[34] suggest that charge density may not be crucial in coacervate formation.

Coacervate Characterization

We exploited a representative (R_5R_5, D_{10}) system and optimized the conditions such as total charge (from peptides, [Arg] + [Asp]), charge ratio ([Arg]/[Asp]), pH, ionic strength (from inorganic salts), and surfactants. In Figure 2c, we observed a slight increase in turbidity at *total charges* of 0.8–3 mM, followed by a substantial rise when exceeding 3 mM. This indicates the formation of numerous droplets. The corresponding DLS measurement showed a similar trend, with a critical total charge of 0.8 mM resulting in a droplet size of 0.1 μm, but less than 10% of the peptide was complexed in the coacervate phase (Table S1). Therefore, we chose a 5 mM total charge for subsequent experiments, which gave coacervate yields more than 90% and a sufficient number of droplets.

Next, Figure 2d shows that the maximum (R_5R_5, D_{10}) coacervation occurred at a *charge stoichiometry* between 0.5 and 1.[35] Charge ratios below 0.5 or above 1 produced little-to-no coacervates. Notably, a closer examination in gel electrophoresis demonstrated that the optimal charge stoichiometry is 0.5 for the ($Cy3$-R_5R_5, $Cy5.5$-D_{10}) system using the dye-labeled peptides, with approximately 100% of the peptides concentrated in coacervates (Figure 2e). Other charge ratios and controls contained free peptide dye that moved toward cathode or anode. The lack of mobility shift observed for the coacervates at 0.5 charge ratio was due to their large size compared to the dimensions of the pores (see well 4, Figure

2e),[31] rather than a charge neutrality. Therefore, the optimal conditions for (R_5R_5, D_{10}) coacervation were found to be a 5 mM total charge and 0.5 charge ratio.

The *size* of coacervates was then characterized by DLS, TEM, and confocal microscope. The fresh coacervates showed a D_H of 0.64 μm with a low polydispersity index of PDI = 0.09, indicative of a homogeneous population of droplets (Figure 2f). Other peptide combinations, such as (R_{10}, D_5D_5), also exhibited coacervates in the (sub)micrometer regime, with an average size of 0.68 μm (Table 2 and Figure S6). TEM images outlined subpopulations of stained coacervates with a size range of 0.4 to 0.8 μm (Figures 2g and S6b). Confocal microscopy was challenging due to rapid movement of droplets, but after aging the samples, most coacervates settled and could be imaged with an average size of 3.0 ± 1.1 μm (Figure 2h). The observed droplet enlargement after aging can be attributed to coalescence facilitated by the fluid-like character of the membraneless system.[16,36]

To enhance colloidal stability and reduce interparticle coalescence, we incorporated the nonionic *surfactant* Tween-20 (0.2% w/v) during the coacervation of (R_5R_5, D_{10}) peptides.[37] The efficacy of this approach was monitored by time-resolved turbidity measurements, as shown in Figure 2i. Compared with the control sample without the surfactant, the introduction of Tween-20 substantially retarded the turbidity decay, with 70% of initial turbidity preserved after 3 h. In contrast, the control sample had a drastic turbidity drop of 80% within 0.5 h, and microscopy showed a bulk liquid instead of well-dispersed droplets (Figure S7). This discrepancy is attributed to the Tween-20 above critical micelle concentration (CMC) acting as non-interacting physical barrier and impedes colliding coalescence of the membraneless droplets. The stabilization by Tween-20 surfactant also held for other coacervates formed from (R_{10}, D_5D_5) and $(R_{10}D_5, D_{10})$ (Figure S7). Gel electrophoresis confirmed that Tween-20 did not affect the droplet integrity (see well 10, Figure 2e). In contrast, ionic surfactants such as sodium dodecyl sulfate (SDS) and cetyltrimethyl ammonium bromide (CTAB), above their CMC, disrupted our complex coacervates by electrostatically competing with the counter polyions (Figure 2e, wells 8 & 9).[29,38] This also confirms that electrostatic interactions are the primary driving force in our system, with limited involvement of the hydrophobic interaction. Taken together, Tween-20 proves to be an alternative and simple means of stabilizing nonmembrane coacervates.[16,36]

pH and ionic strength are crucial factors that determine the outcome of coacervation. In Figure 2j, a pH range of 6–14 is essential for the coacervation of (R_5R_5, D_{10}) peptides because deprotonation of the carboxyl in Asp occurs above p$K_a \approx 3.9$.[39] However, overly basic conditions hinder coacervation, likely due to the deprotonation of the guanidinium group in Arg (p$K_a \approx 13.8$)[40] and high ionic strength. Therefore, the optimal pH range for favorable (R_5R_5, D_{10}) coacervation is near the physiological range, in line with previous studies.[19]

In terms of *ionic strength*, it is widely acknowledged that low ionic strength favors complex coacervation, as demonstrated in our empirical correlation between the maximum NaCl concentration and total charge of coacervates by $[NaCl]_{max} \approx [total\ charge] \times 10$ (Figure S7g). The phase diagrams in Figures 2j and S7g were constructed by mixing preconditioned peptide solutions. However, it is worth mentioning that once formed, $(R_5R_5,$

D_{10}) coacervates displayed stability at a wide range of pH 2–14 and NaCl concentrations (0–200 mM). This is attributed to the robust electrostatic interactions conferred by the oligoarginines.[15,25] The salt stability of (R_5R_5, D_{10}) coacervates is specific to NaCl because sub-millimolar concentrations of $CaCl_2$ rapidly cross-link and aggregate the droplets (Figure S7h).[30,41] In summary, we optimized a phosphate buffer (20 mM, pH 8.0) without NaCl but with 0.2% (w/v) Tween-20 to investigate the interactions between the coacervate and M^{pro}.

Proteases Interact with Nonfluorescent Coacervates

We asked whether M^{pro} interacts with the R_5R_5 substrate trapped within the (R_5R_5, D_{10}) coacervates. To prepare the coacervate samples, the peptides were thoroughly mixed in a transparent cuvette for 10 s, and the resulting turbid dispersion was photographed for every 30 s. Other conditions used 5 mM total charge, 0.5 charge ratio, 20 mM PB (pH 8), 0.2% Tween-20, and a substrate-to-enzyme ratio of 800:1. In Figure 2k, the addition of 200 nM M^{pro} to the opaque emulsion led to a clear solution in 5.5 min. This provided compelling evidence of the protease cleaving the trapped R_5R_5 substrate and producing fragments that are incapable of sustaining the requisite charge valency necessary for continued coacervation.

The control trial without M^{pro} remained turbid. The coacervates constituting scramble sequences r_5r_5 and M^{pro} also showed no turbidity drop, indicating the need for specific recognition between substrate and protease. Other coacervates, including (D_5D_5, R_{10}), also showed enzyme responsiveness, as evidenced by the additional mass data of the substrate fragments (Figure S3b).

The turbidity dynamics during a proteolysis was further corroborated with molecular dynamics (MD) simulations to elucidate the microscale interactions between D_{10} and R_5R_5 peptides. Two systems were simulated: system one with 20 D_{10} and 10 intact R_5R_5 peptides and system two with 20 D_{10} and 10 peptide fragments. The peptide mixture formed one large cluster within 25 ns in system one, while small peptidic clumps were slowly formed in system two (Figure S8). The solvent-accessible surface area (SASA) decreased more rapidly in system one, resulting in a smaller SASA value at equilibrium. In addition, system one displayed fewer peptide-water hydrogen bonds, indicating prevalent ion-pairing interactions within peptide aggregates that depleted the charged groups (Figure S8). These results suggest that the interactions between D_{10} and intact R_5R_5 are stronger than those after proteolysis, favoring coacervation and stressing the role of critical charge valency.

Enzyme Modeling with Self-Quenching-Based Coacervates

Coacervates exhibit a confinement structure and favor energy transfer-based transductions by bringing interacting moieties into close proximity. This has been exploited by other groups to study the inter- and intracoacervate associations.[15,42] However, the subsequent dissolution of coacervates has received little attention, which also impacts the separation distance and energy transfer. Here, we used a dye-labeled peptide in the (Cy5.5-R_5R_5, D_{10}) coacervates and realized a self-quenching (or contact quenching[43,44]) effect resulting from an increase in the local dye concentration, reaching approximately 100-fold based on related work.[4,15,45] We also observed that integration of Cy5.5 dye to the coacervate led to

a reduction in the critical total charge from 0.8 mM for (R_5R_5, D_{10}) to 0.024 mM (Figure 2c). This is presumably due to additional cation-π interactions that reinforce interpeptide association. Subsequent M^{pro} addition disassembled the coacervates, recovered the dye PL, and allowed for the modeling of enzyme kinetics.

Figure 3a,b shows the immediate optical differences of Cy5.5 upon incorporation into coacervate. The introduction of 1% w/v SDS (above CMC) to coacervates is 2-fold: (i) it breaks the ion-pairing interactions and disassembles the coacervates,[29] and (ii) it minimizes dye–dye stacking interactions and favors its monomeric state.[38,46] The absorbance peak wavelength (λ_{max}) of Cy5.5 in coacervates blue-shifts from 687 nm for the monomeric dye to 677 nm, indicating strong intermolecular interactions of Cy5.5.[44] This shift is accompanied by the intensity reductions of the hypochromic peak and peak broadening. The PL peak wavelength also exhibits a 20 nm hypochromic shift along with a high PL quenching efficiency of 93%. This efficiency is calculated using $E\% = 1 - PL_{coacervate}/PL_{free}$. Meanwhile, the photoacoustic (PA) response of (Cy5.5-R_5R_5, D_{10}) coacervates was studied by using pulsed laser irradiation ($\lambda = 680$ nm) to generate pressure transients and ultrasound signals. In Figure 3c, the coacervates show a 2- to 4-fold PA enhancement over the disassembled samples across three tested dye concentrations. This correlation is attributed to the energy dissipation via nonradiative decay (or heat) following light absorption.[46] The decrease in the quantum yield (QY) from 0.16 for the free dye to 0.05 also supports the observed PL quenching (Table S2). Our group has reported near-complete self-quenching of the dye PL and enhanced PA signal through aggregation-associated interactions, realized by bringing a dye dimer in close proximity using a short linker.[44] Furthermore, we confirmed that Cy5.5 can be replaced with other dyes (e.g., Cy3) while still providing sufficient PL quenching for triggered PL recovery.

Next, we monitored the reaction of M^{pro} (200 nM) on the fluorogenic coacervates with varying total charges ranging from 0.024 to 0.8 mM. The PL at 720 nm ($PL_t - PL_0$) was recorded for 2 h at 37 °C and pH 8. By modulating the total charges, we could simultaneously adjust the substrate concentrations ranging from 0.8 to 26.6 μM. Figure 3d,e shows that the enhancement in the $PL_{720\ nm}$ with time is commensurate with the R_5R_5 employed. Up to 2.7-fold PL recovery was measured at a substrate concentration of 16 μM (Figure S9b). The control showed no PL enhancement under identical conditions in the absence of M^{pro} (Figure S9c). Therefore, we selected a substrate concentration of 16 μM for further study, unless otherwise indicated.

The progressive increase in PL demonstrates that the digestion of the (Cy5.5-R_5R_5, D_{10}) coacervates releases the dye from the droplets. The data in Figure 3e were further converted to the amount of cleaved Cy5.5-R_5R_5 for quantification of the kinetic parameters. To do this, we retrieved the proteolyzed samples at 12 h and quantified the dye amount in the supernatant (i.e., fragment). A linear standard curve was found between the PL and the dye fragment concentration (Figure S9). This linear fit was then used to back-calculate the amount of product in the real-time proteolysis and build a classical Michaelis–Menten (MM) plot. Our results show that M^{pro} can digest up to 75% of the coacervates, while the undigested part can be attributed to the bulk phase induced by coalescence and sedimentation, where the substrate is inaccessible to protease (Table 3).

The specificity constant, k_{cat}/K_M, for the (Cy5.5-R_5R_5, D_{10}) coacervates by M^{pro} was 5817 M^{-1} s^{-1}, as shown in the MM curve in Figure 3f. This finding provides valuable insights into the interactions between nonmembrane droplets and enzymes, as a comparison of k_{cat}/K_M for the substrate in coacervate versus in solution has not been previously reported. To address this, we further measured the k_{cat}/K_M for free substrate by M^{pro} using a synthetic peptide (Cy5.5–R_5R_5C–Cy3, Figure S10) and obtained a value of 5159 M^{-1} s^{-1}. This value is slightly or 1.1-fold lower than that of coacervates. The fact that both systems exhibited a similar K_M value of 10 μM indicates that M^{pro} binds to the substrate with a comparable affinity irrespective of the coacervates.[49] The obtained specificity constants are consistent with prior findings, and slight differences may arise from variations in assay conditions or customization in the substrate sequences (Table 3).[41,50]

Our findings are not unusual because enzyme kinetics on a scaffold (e.g., particle or membrane) have been a topic of debate, with some supporting a slow kinetic model that considers slow diffusion and steric crowdedness,[51,52] while others favor a fast kinetic model that emphasizes enzyme hopping and high local concentration.[53] On the one hand, our finding agrees with a recent study by Keating et al., showing that phosphatase exhibits slightly higher activity toward substrates within coacervates compared to free substrates, and kinase activity was not significantly altered by the presence of coacervates.[9] On the other hand, we must stress that the protease solely needs to reduce the substrate level below the critical total charge to fully recover the PL signal instead of complete digestion, which leads to a large apparent k_{cat}/K_M value.

Inhibition, Specificity, and Matrix Effects

The observation that the (Cy5.5-R_5R_5, D_{10}) coacervates have a characteristic specificity constant with M^{pro} presents a promising platform for enzyme studies. To estimate the limit of detection (LoD), increasing amounts of M^{pro} from 0–500 nM were incubated with (Cy5.5-R_5R_5, D_{10}) coacervates containing a fixed amount of substrate at 16 μM. Figure 3g indicates that higher M^{pro} concentration resulted in more PL recovery and *vice versa*. Figure 3h shows the $PL_{720\,nm}$ as a function of the M^{pro} concentration at 1 h readout time: The LoD was determined to be 55.7 nM, following a previously established method.[47] This LoD is 2-fold higher than that of our previous colorimetric sensors due to the short readout time of the current system.[29]

The observed PL recovery resulting from specific proteolysis was validated through the inhibition assays. For example, M^{pro} (200 nM) was incubated with GC376 inhibitor at varying molar ratios ([I]/[E] = 0–10) for 10 min before mixing with (Cy5.5-R_5R_5, D_{10}) coacervates containing 16 μM substrate. In Figure 3i, higher amounts of inhibitor resulted in slower enzymatic reactions and PL recovery, with a 10-fold excess of GC376 inhibiting the protease activity. This excludes the PL recovery by nonspecific interactions between the coacervates and M^{pro}. A closer examination of the $PL_{720\,nm}$ at 30 min yields a typical inhibitor titration curve (Figure 3j). The Henderson equation (Eq. S11) estimated the active M^{pro} fraction to be 70%, and the potency of GC376 inhibitor is $K_{i\,(app)} = 138$ nM and half-maximal inhibitory concentration (IC_{50}) = 208 nM. These values agree with previous findings.[54-56] To this end, the specificity of (Cy5.5-R_5R_5, D_{10}) coacervates was evaluated

toward other proteins (200 nM), including trypsin, thrombin, α-amylase (200 U/mL[48]), bovine serum albumin (BSA), and hemoglobin. In Figure 3k, no PL activation was detected in the presence of BSA, hemoglobin, or other enzymes, except for trypsin, which led to an undesired signal higher than that of M[pro]. This is not surprising since trypsin cleaves the C-terminal of Arg, and the R_5R_5 substrate contains multiple potential cleavage sites.[29,49]

We evaluated matrix effects by spiking the (Cy5.5-R_5R_5, D_{10}) coacervates in PB buffer, exhaled breath condensate (EBC),[29] urine, Dulbecco's Modified Eagle's Medium (DMEM) cell culture media, BSA solution (1% w/v), human pooled saliva,[48] and human plasma.[57] We first assessed the stability of (Cy5.5-R_5R_5, D_{10}) coacervates in the above matrices. The coacervates showed good stability without PL changes in the buffer, EBC, urine, and saliva. Nonetheless, these coacervates showed rapid dissolution in high concentrations of BSA and were prone to competitive binding with constituents in cell growth media and human plasma, thus leading to fully recovered PL prior to the onset of proteolysis (Figure S11).[58] Subsequently, 200 nM M[pro] was introduced to the coacervates in buffer, EBC, urine, and saliva, and the time-dependent PL recovery was recorded (Figure S12). Figure 3l shows the relative PL changes at 20 min in various matrices by establishing a complete PL recovery in buffer as the topline. The coacervate-enzyme interactions were maintained in the buffer, EBC, and urine. The coacervates in saliva showed a 19% PL recovery independent of M[pro] addition (Figure S12e), possibly due to nonspecific interactions or other proteases such as Arg-gingipains implicated in periodontal disease.[59]

Other Signal Transduction Mechanisms

The self-quenching approach proposed in this study exploits the spatial proximity of dye molecules within complex coacervates, thereby offering a viable avenue for implementing FRET and AIE mechanisms. It remains unclear, however, whether the kinetics of M[pro] on the designed coacervates would be consistent with those of the previously examined (Cy5.5-R_5R_5, D_{10}) droplets, given the distinct types and quantities of dyes employed.

The FRET mechanism was exploited using a Cy3-Cy5.5 donor–acceptor pair, leading to (Cy3-R_5R_5, Cy5.5-D_{10}) coacervates with notable alterations in their optical properties. For example, the absorption profile showed a red-shifted λ_{max} with a reduction in peak intensity, and the PL profile exhibited a substantial donor quenching with an efficiency more than 99.9% (Figure S13). FRET theory estimated the Cy3-Cy5.5 distance within the coacervates to be no greater than 1.3 nm, given that an acceptor-to-donor ratio is 2, an overlap integral for Cy3-Cy5.5 pair is 3.4×10^{-13} M^{-1} cm^3, a Förster distance (R_0) is 3.7 nm,[49] and a measured E_{FRET} is 99.9% (Eq. S5).[60] This suggests a concentrated peptide-dye within individual droplets. We then monitored the PL$_{560 nm}$ for M[pro] (600 nM) interacting with the (Cy3-R_5R_5, Cy5.5-D_{10}) coacervates at various total charges (0.024–1.2 mM). Figure 4a shows that more PL recovery of the Cy3 donor is observed for higher substrate concentration, implying that M[pro] releases the coupled Cy3 from the droplets. However, the attainment of kinetic equilibrium required an hour-scale time and resulted in a low digestion yield of 5% (Table 3). In Figure 4b, the (Cy3-R_5R_5, Cy5.5-D_{10}) coacervates with M[pro] exhibited a k_{cat}/K_M of 259 M^{-1} s^{-1}, which was about 20-fold lower than that of the free substrate (Table 3).[41,50]

The AIE-based coacervates were designed and made using the conjugated PMR peptide with PyTPE luminogen (Table 1).[28,61] The coacervation of (PMR, D_{10}) led to 4.5-fold enhancement in PL compared with that of free PMR peptide (Figure S13e). Subsequent addition of M^{pro} to the AIE coacervates induced a decrease in PL intensity. To streamline data analysis in a signal recovery format, the PL decay induced by M^{pro} was reversed by subtracting the real-time PL signal from that of the control. Figure 4c shows the PL changes of AIE coacervates at various PMR concentrations at 200 nM of M^{pro}. A simple and alternative kinetic analysis was adapted by fitting Figure 4c with the time-integrated MM equation (Eq. S7) and extracting the first-order rate constant, K_{obs}. The K_{obs} was then correlated with the specificity constant by $K_{obs} = k_{cat}[E]/K_M$.[52] This yielded the k_{cat}/K_M of 1208 M^{-1} s^{-1}, which is about 4-fold less than that of the free substrate (Figure S10).[41,50] Figure 4d indicates that the K_M is 10.6 μM. The lower kinetics also manifested in a total of 20% reduction in PL, whereas a complete dissolution of the AIE coacervates would correspond to an 80% reduction in PL (Figure S13). In addition, we examined another AIE system using (PyTPE-R_5R_5, D_{10}) and found no PL enhancement, presumably due to the dysregulation of the close pack of PyTPE luminogen by the nearby charged R_5 domain within the droplets (Figure S2f),[62] suggesting that further studies are needed to comprehend the optimal design of AIE substrates within a liquid-like phase.

The distinct kinetics observed among the three sets of the fluorogenic coacervates and M^{pro} provide initial proof of the effects of hydrophobicity (e.g., via dye type and quantity) on the bioactivity of coacervates (Table 3). To further test the impact of dye quantity, we carried out an additional experiment involving the introduction of extra Cy5.5 to the self-quenching-based (Cy5.5-R_5R_5, Cy5.5-D_{10}) coacervates. Similar changes in optical profiles were obtained as with the above (Cy5.5-R_5R_5, D_{10}) system (Figure S13h,i). However, the introduction of M^{pro} to the (Cy5.5-R_5R_5, Cy5.5-D_{10}) samples showed no PL recovery, with the intensity remaining constant for over 3 h (Figure S13k). The control without M^{pro} yielded the same result. Referring to Table 3, the decrease in specificity constant of various systems was primarily attributed to a decrease in turnover number (k_{cat}), while K_M remained at a similar level (5–15 μM). This behavior resembles to noncompetitive inhibition, where the inhibitor binds to a nonactive site of the enzyme. We thus suggest that the inclusion of larger hydrophobic moieties in (R_5R_5, D_{10}) coacervates is likely to bind to the hydrophobic domain of M^{pro}, distinct from the active site, resulting in a decrease in enzyme kinetics. A few additional modifications can be done to provide a comprehensive understanding of the coacervates by enzyme. These modifications include, among others: (i) Inclusion of varying portion of aromatic amino acids in the complexing peptides. (ii) Use of polyions with varying molecular weight. (iii) Tethering of hydrophilic fluorophores. (iv) Integration of a surface coating layer. (v) Inclusion of multiple substrates in coacervates (Figure S14).[63]

Enzyme Releases the Payload in Coacervates

We briefly evaluate the capability of (R_5R_5, D_{10}) complex coacervates in encapsulation and subsequent M^{pro}-mediated release of payload.[6] As a proof of concept, fluorescent materials (100 μM) were studied as the representative model due to their easy visualization under a confocal microscope.

For example, the cationic dyes [e.g., azure A, azure C, methylene blue (MB), rhodamine B (RB), and rhodamine 6G (R6G)] and hydrophobic dye (neutral red) were largely partitioned into the coacervates (Figures 5 and S15). In comparison, a significant variation in the partition process was observed for anionic materials [e.g., fluoresceine, ICG dye, green fluorescence protein (GFP), and diphenylphosphino-benzene-3-sulfonate (DPPS)-modified Au/Ag nanoclusters (NCs)[41,64]]. The encapsulation efficiency (EE%) and partition coefficient (K) of the dyes are summarized in Table 4. The results indicate that cationic and hydrophobic dyes were preferentially sequestered (EE% > 50%). This is because the (R_5R_5, D_{10}) coacervates carry net negative charges ($\zeta = -6.2 \pm 0.8$ mV), favoring electrostatic attractions with cationic molecules. Meanwhile, the R_5R_5 constituent also shows favorable cation-π interactions with molecules rich in aromatic moieties and benefits their solubility in water. This is demonstrated by the highest K value of 13.9 realized with a neutral red (Figure 5b). However, the negatively charged dyes showed limited interactions with our coacervates; e.g., less than 10% of fluoresceine was internalized (Figure 5c). Subsequently, the addition of M^{pro} to these dye-encapsulated coacervates resulted in near complete dye release, as suggested in Figure 2k and Table 4. These combined observations suggest that (R_5R_5, D_{10}) coacervates possess selective solute sequestration and release efficiency upon enzymatic stimuli.

We also show that red-emitting inorganic Au/Ag NCs coated with DPPS preferentially accumulate on the (R_5R_5, D_{10}) coacervate surfaces. These water-soluble NCs were less or not observed inside the coacervates likely due to their large size (1–2 nm[64]) and steric hindrance,[65] thus resulting in bright and hollow circles under confocal microscopy (Figure 5d). The addition of the other solutes such as ICG dye, doxorubicin, and GFP rapidly cause transformation of coacervates into solid aggregates (Figure S15).[35,42] Finally, the *in vitro* toxicity test revealed that the complex coacervate (up to 2 mM total charge) and individual peptides exerted negligible impact on cell viability (Figure S16), thus highlighting their potential for low cytotoxicity in triggered delivery applications, contingent upon optimized colloidal stability and release kinetics.[66]

CONCLUSION

In summary, we have modeled the interactions between complex coacervates and the main protease. We found that the fluorescence self-quenched and submicron coacervates have minimal effect on the interacting kinetics between the embedded substrate and soluble M^{pro}. We also found that the enzyme-coacervate interactions depend on the specific nature of the droplets such as the type and quantity of dye integrated, with doubling the amount of dye essentially quenching the proteolysis reactions. Specifically, the nonmembrane coacervates constitute of R_5R_5 and D_{10}. We first identified several optimal conditions for coacervation: (i) The lowest charge valence for Arg-peptide was 10, given D_{10} as the counter polyanion. (ii) The critical total charge was 0.8 mM. (iii) The exact charge ratio was 0.5 for 100% of peptide complexation. (iv) pH above 6 was required. (v) A 0.2% nonionic Tween-20 enhanced the stability. Three signal transductions were applied to the coacervates, including self-quenching, FRET, and AIE mechanisms. The k_{cat}/K_M extracted from the self-quenching (Cy5.5-R_5R_5, D_{10}) was 5817 M^{-1} s^{-1}, which is 1.1-fold higher than that of free substrate. This work presents a simple design of enzyme-responsive coacervates

and provides informative insights into the interactions between the enzyme and complex coacervates as substrate hub.

EXPERIMENTAL SECTION

Materials

Fmoc-protected amino acids, hexafluorophosphate benzotriazole tetramethyl uronium (HBTU), and Fmoc-Rink amide MBHA resin (0.67 mmol/g, 100–150 mesh) were purchased from AAPPTec, LLC (Louisville, KY). Fmoc-L-propargylglycine (Pra) was obtained from Combi Blocks Inc. (San Diego, CA). The recombinant SARS-CoV-2 main protease (M^{pro}) was expressed using the M^{pro} plasmid provided by Prof. Rolf Hilgenfeld, University of Lübeck, Germany and purified as previously described.[50] The *N*-hydroxysuccinimide (NHS)-ester dyes were purchased from Lumiprobe Corp. (Hunt Valley, MD). Ultrapure water (18 MΩ·cm) was obtained from a Milli-Q Academic water purification system (Millipore Corp., Billerica, MA).

Peptide Synthesis

Peptides were chain assembled by Fmoc-SPPS (solid-phase peptide synthesis) on Rink-amide-MBHA-resin (0.67 mmol/g, 200 mg) following our previous protocol using an automated Eclipse peptide synthesizer (AAPPTec, Louisville, KY).[41] The synthetic peptides were cleaved from the resin using a cleavage cocktail (3 mL) that contained trifluoroacetic acid (TFA) (82.5%), EDDET (2.5%), phenol (5%), thioanisole (5%), and H_2O (5%). Resins were treated with the cleavage cocktail for 10–12 h with gentle shaking to ensure a full cleavage of side-chain protection groups. The peptides were purified by reversed-phase high-performance liquid chromatography (HPLC) (Shimadzu LC-40), confirmed by matrix-assisted laser desorption/ionization time-of-flight mass spectrometry (MALDI-TOF MS), aliquoted ($\varepsilon_{205} = 31$ mL·mg^{-1}·cm^{-1}) using a NanoDrop One UV–vis spectrophotometer (Thermo Fisher Scientific), and stored in dry conditions at room temperature for further use.

Cy5.5-Labeled Peptides

An aqueous solution of D_{10} peptide (3.0 mg or 2.6 μmol, in 1 mL of PB, pH 8.0) was mixed with NHS-Cy5.5 (1.0 mg or 1.3 μmol, in 1.5 mL of dimethyl sulfoxide (DMSO)); the final pH of the mixture was adjusted to ~8 using NaOH solution (1 M) if needed. The reaction was stirred for 1 h protected from light, followed by drying in a speed vacuum system at 60 °C. The conjugation yield was ~40% after HPLC purification; see MALDI-TOF MS data in Figure S2.

Coacervates Preparation

The complex coacervates (60 μL) were prepared by thoroughly mixing the desired amount of negatively charged peptides, PB buffer (20 mM, pH 8.0), and positively charged peptides in order at room temperature. Coacervate formation was initially examined by an optical microscope (40×) on an EVOS XL Core imaging System (Thermo Fisher Scientific). The fluorogenic coacervates were typically studied at total charges of 0.48 mM (e.g., for detection limits) and 0.8 mM (e.g., for studying photophysical properties). For example, the conditions of R_5R_5-Cy5.5 and D_{10} at 0.5 charge ratio and 0.48 mM total charge used the D_{10}

(2.1 mM, 0.92 μL), PB (20 mM, pH 8.0, 0.2% Tween-20, 54.7 μL), and R_5R_5-Cy5.5 (0.78 mM, 1.2 μL) in order.

Proteolysis on Self-Quenching Coacervates

A series of coacervates (charge ratio = 0.5, pH 8, 0.2% Tween-20, 60 μL) with various total charges (i.e., 0.024, 0.08, 0.16, 0.24, 0.48, 0.8, and 1.2 mM) were prepared by thoroughly mixing a desirable amount of D_{10} (2.1 mM in PB, pH 8), PB (20 mM, pH 8, 0.2% Tween-20), and R_5R_5-Cy5.5 (0.78 mM in PB, pH 8) in order in a 96-well plate. This corresponds to a final *substrate concentration* (here, $[S]_0$, or $[R_5R_5$-Cy5.5]) of 0.8, 2.7, 5.3, 8.0, 16, 26.6, and 39.4 μM. The resulting coacervates were then preincubated at 37 °C for 20 min using a hybrid multimode microplate reader to stabilize the PL signal. Next, the desired amount of M^{pro} ($[M^{pro}]_{final}$ = 200 nM, 70% active) was added to each well, and the mixture was thoroughly pipetted. The plate was immediately sealed and incubated at 37 °C in the hybrid multimode microplate reader with 3 s of shaking before each cycle of reading, and the PL intensity (excitation/emission wavelength = 630 nm/720 nm) was recorded over 12 h with 1 min intervals between each cycle. Control used the same protocol without introducing M^{pro}. Experiment was done in triplicate.

Supplementary Material

Refer to Web version on PubMed Central for supplementary material.

ACKNOWLEDGMENTS

REFERENCES

(1). Brangwynne CP; Eckmann CR; Courson DS; Rybarska A; Hoege C; Gharakhani J; Jülicher F; Hyman AA Germline P Granules Are Liquid Droplets That Localize by Controlled Dissolution/Condensation. Science 2009, 324, 1729–1732. [PubMed: 19460965]

(2). Yang P; Mathieu C; Kolaitis R-M; Zhang P; Messing J; Yurtsever U; Yang Z; Wu J; Li Y; Pan Q; Yu J; Martin EW; Mittag T; Kim HJ; Taylor JP G3BP1 Is a Tunable Switch that Triggers Phase Separation to Assemble Stress Granules. Cell 2020, 181, 325–345. [PubMed: 32302571]

(3). Xu C; Martin N; Li M; Mann S Living material assembly of bacteriogenic protocells. Nature 2022, 609, 1029–1037. [PubMed: 36104562]

(4). Hughes MP; Sawaya MR; Boyer DR; Goldschmidt L; Rodriguez JA; Cascio D; Chong L; Gonen T; Eisenberg DS Atomic structures of low-complexity protein segments reveal kinked beta-sheets that assemble networks. Science 2018, 359, 698–701. [PubMed: 29439243]

(5). Mu W; Ji Z; Zhou M; Wu J; Lin Y; Qiao Y Membrane-confined liquid-liquid phase separation toward artificial organelles. Sci. Adv 2021, 7, eabf9000. [PubMed: 34049872]

(6). Sun Y; Lau SY; Lim ZW; Chang SC; Ghadessy F; Partridge A; Miserez A Phase-separating peptides for direct cytosolic delivery and redox-activated release of macromolecular therapeutics. Nat. Chem 2022, 14, 274–283. [PubMed: 35115657]

(7). Zhang P; Fan B; Yang P; Temirov J; Messing J; Kim HJ; Taylor JP Chronic optogenetic induction of stress granules is cytotoxic and reveals the evolution of ALS-FTD pathology. eLife 2019, 8, e39578. [PubMed: 30893049]

(8). Kubota R; Torigoe S; Hamachi I Temporal Stimulus Patterns Drive Differentiation of a Synthetic Dipeptide-Based Coacervate. J. Am. Chem. Soc 2022, 144, 15155–15164. [PubMed: 35943765]

(9). Aumiller WM; Keating CD Phosphorylation-mediated RNA/peptide complex coacervation as a model for intracellular liquid organelles. Nat. Chem 2016, 8, 129–137. [PubMed: 26791895]

(10). Wang T; Tian X; Kim HB; Jang Y; Huang Z; Na CH; Wang J Intracellular energy controls dynamics of stress-induced ribonucleoprotein granules. Nat. Commun 2022, 13, 5584. [PubMed: 36151083]

(11). Escalante LE; Gasch AP The role of stress-activated RNA-protein granules in surviving adversity. RNA (New York, N.Y.) 2021, 27, 753–62. [PubMed: 33931500]

(12). Schütz S; Nöldeke ER; Sprangers R A synergistic network of interactions promotes the formation of in vitro processing bodies and protects mRNA against decapping. Nucleic Acids Res. 2017, 45, 6911–6922. [PubMed: 28472520]

(13). Boeynaems S; Alberti S; Fawzi NL; Mittag T; Polymenidou M; Rousseau F; Schymkowitz J; Shorter J; Wolozin B; Van Den Bosch L; Tompa P; Fuxreiter M Protein Phase Separation: A New Phase in Cell Biology. Trends Cell Biol. 2018, 28, 420–435. [PubMed: 29602697]

(14). Liu J; Tian L; Qiao Y; Zhou S; Patil AJ; Wang K; Li M; Mann S Hydrogel-Immobilized Coacervate Droplets as Modular Microreactor Assemblies. Angew. Chem., Int. Ed 2020, 59, 6853–6859.

(15). Choi S; Meyer MO; Bevilacqua PC; Keating CD Phase-specific RNA accumulation and duplex thermodynamics in multiphase coacervate models for membraneless organelles. Nat. Chem 2022, 14, 1110–1117. [PubMed: 35773489]

(16). Zhang Y; Chen Y; Yang X; He X; Li M; Liu S; Wang K; Liu J; Mann S Giant Coacervate Vesicles As an Integrated Approach to Cytomimetic Modeling. J. Am. Chem. Soc 2021, 143, 2866–2874. [PubMed: 33566601]

(17). Lu T; Spruijt E Multiphase Complex Coacervate Droplets. J. Am. Chem. Soc 2020, 142, 2905–2914. [PubMed: 31958956]

(18). Lu T; Liese S; Schoenmakers L; Weber CA; Suzuki H; Huck WTS; Spruijt E Endocytosis of Coacervates into Liposomes. J. Am. Chem. Soc 2022, 144, 13451–13455. [PubMed: 35878395]

(19). Abbas M; Lipiński WP; Nakashima KK; Huck WTS; Spruijt E A short peptide synthon for liquid–liquid phase separation. Nat. Chem 2021, 13, 1046–1054. [PubMed: 34645986]

(20). Guindani C; da Silva LC; Cao S; Ivanov T; Landfester K Synthetic Cells: From Simple Bio-Inspired Modules to Sophisticated Integrated Systems. Angew. Chem., Int. Ed 2022, 61, e2021–10855.

(21). Li P; Banjade S; Cheng H-C; Kim S; Chen B; Guo L; Llaguno M; Hollingsworth JV; King DS; Banani SF; Russo PS; Jiang Q-X; Nixon BT; Rosen MK Phase transitions in the assembly of multivalent signalling proteins. Nature 2012, 483 (7389), 336–340. [PubMed: 22398450]

(22). Abbas M; Lipiński WP; Wang J; Spruijt E Peptide-based coacervates as biomimetic protocells. Chem. Soc. Rev 2021, 50, 3690–3705. [PubMed: 33616129]

(23). Zhou H-X; Pang X Electrostatic Interactions in Protein Structure, Folding, Binding, and Condensation. Chem. Rev 2018, 118, 1691–1741. [PubMed: 29319301]

(24). Lafontaine DLJ; Riback JA; Bascetin R; Brangwynne CP The nucleolus as a multiphase liquid condensate. Nat. Rev. Mol. Cell Biol 2021, 22, 165–182. [PubMed: 32873929]

(25). Cakmak FP; Choi S; Meyer MO; Bevilacqua PC; Keating CD Prebiotically-relevant low polyion multivalency can improve functionality of membraneless compartments. Nat. Commun 2020, 11, 5949. [PubMed: 33230101]

(26). Owen DR; Allerton CMN; Anderson AS; Aschenbrenner L; Avery M; Berritt S; Boras B; Cardin RD; Carlo A; Zhu Y; et al. An oral SARS-CoV-2 Mpro inhibitor clinical candidate for the treatment of COVID-19. Science 2021, 374, 1586–1593. [PubMed: 34726479]

(27). Jin Z; Du X; Xu Y; Deng Y; Liu M; Zhao Y; Zhang B; Li X; Zhang L; Yang H; et al. Structure of Mpro from SARS-CoV-2 and discovery of its inhibitors. Nature 2020, 582, 289–293. [PubMed: 32272481]

(28). Cheng Y; Clark AE; Zhou J; He T; Li Y; Borum RM; Creyer MN; Xu M; Jin Z; Zhou J; Yim W; Wu Z; Fajtová P; O'Donoghue AJ; Carlin AF; Jokerst JV Protease-Responsive Peptide-Conjugated Mitochondrial-Targeting AIEgens for Selective Imaging and Inhibition of SARS-CoV-2-Infected Cells. ACS Nano 2022, 16, 12305–12317. [PubMed: 35878004]

(29). Jin Z; Mantri Y; Retout M; Cheng Y; Zhou J; Jorns A; Fajtova P; Yim W; Moore C; Xu M; Creyer MN; Borum RM; Zhou J; Wu Z; He T; Penny WF; O'Donoghue AJ; Jokerst JV A Charge-Switchable Zwitterionic Peptide for Rapid Detection of SARS-CoV-2 Main Protease. Angew. Chem., Int. Ed 2022, 61, e202112995.

(30). Chang Y-C; Jin Z; Li K; Zhou J; Yim W; Yeung J; Cheng Y; Retout M; Creyer MN; Fajtová P; He T; Chen X; O'Donoghue AJ; Jokerst JV Peptide valence-induced breaks in plasmonic coupling. Chem. Sci 2023, 14, 2659–2668. [PubMed: 36908948]

(31). Viovy J-L Electrophoresis of DNA and other polyelectrolytes: Physical mechanisms. Rev. Mod. Phys 2000, 72, 813–872.

(32). Yang M; Digby ZA; Chen Y; Schlenoff JB Valence-induced jumps in coacervate properties. Sci. Adv 2022, 8, eabm4783. [PubMed: 35584213]

(33). Welsh TJ; Krainer G; Espinosa JR; Joseph JA; Sridhar A; Jahnel M; Arter WE; Saar KL; Alberti S; Collepardo-Guevara R; Knowles TPJ Surface Electrostatics Govern the Emulsion Stability of Biomolecular Condensates. Nano Lett. 2022, 22, 612–621. [PubMed: 35001622]

(34). Iglesias-Artola JM; Drobot B; Kar M; Fritsch AW; Mutschler H; Dora Tang TY; Kreysing M Charge-density reduction promotes ribozyme activity in RNA–peptide coacervates via RNA fluidization and magnesium partitioning. Nat. Chem 2022, 14, 407–416. [PubMed: 35165426]

(35). Blocher McTigue WC; Perry SL Protein Encapsulation Using Complex Coacervates: What Nature Has to Teach Us. Small 2020, 16, 1907671.

(36). Mason AF; Buddingh' BC; Williams DS; van Hest JCM Hierarchical Self-Assembly of a Copolymer-Stabilized Coacervate Protocell. J. Am. Chem. Soc 2017, 139, 17309–17312. [PubMed: 29134798]

(37). Bos R; Rutten L; van der Lubbe JEM; Bakkers MJG; Hardenberg G; Wegmann F; Zuijdgeest D; de Wilde AH; Koornneef A; Verwilligen A; van Manen D; Kwaks T; Vogels R; Dalebout TJ; Myeni SK; Kikkert M; Snijder EJ; Li Z; Barouch DH; Vellinga J; Langedijk JPM; Zahn RC; Custers J; Schuitemaker H Ad26 vector-based COVID-19 vaccine encoding a prefusion-stabilized SARS-CoV-2 Spike immunogen induces potent humoral and cellular immune responses. NPJ. Vaccines 2020, 5, 91. [PubMed: 33083026]

(38). Wang J; Lin C-Y; Moore C; Jhunjhunwala A; Jokerst JV Switchable Photoacoustic Intensity of Methylene Blue via Sodium Dodecyl Sulfate Micellization. Langmuir 2018, 34, 359–365. [PubMed: 29232146]

(39). Harms MJ; Castañeda CA; Schlessman JL; Sue GR; Isom DG; Cannon BR; García-Moreno B The pK(a) values of acidic and basic residues buried at the same internal location in a protein are governed by different factors. J. Mol. Biol 2009, 389, 34–47. [PubMed: 19324049]

(40). Fitch CA; Platzer G; Okon M; Garcia-Moreno B; McIntosh LP Arginine: Its pKa value revisited. Protein Sci. 2015, 24, 752–761. [PubMed: 25808204]

(41). Jin Z; Li Y; Li K; Zhou J; Yeung J; Ling C; Yim W; He T; Cheng Y; Xu M; Creyer MN; Chang Y-C; Fajtová P; Retout M; Qi B; Li S; O'Donoghue AJ; Jokerst JV Peptide Amphiphile Mediated Co-assembly for Nanoplasmonic Sensing. Angew. Chem., Int. Ed 2023, 135, e202214394.

(42). Vieregg JR; Lueckheide M; Marciel AB; Leon L; Bologna AJ; Rivera JR; Tirrell MV Oligonucleotide–Peptide Complexes: Phase Control by Hybridization. J. Am. Chem. Soc 2018, 140, 1632–1638. [PubMed: 29314832]

(43). Kumar Panigrahi S; Kumar Mishra A Inner filter effect in fluorescence spectroscopy: As a problem and as a solution. J. Photochem. Photobiol. C: Photochem. Rev 2019, 41, 100318.

(44). Moore C; Borum RM; Mantri Y; Xu M; Fajtová P; O'Donoghue AJ; Jokerst JV Activatable Carbocyanine Dimers for Photoacoustic and Fluorescent Detection of Protease Activity. ACS Sens. 2021, 6, 2356–2365. [PubMed: 34038103]

(45). Li L; Srivastava S; Andreev M; Marciel AB; de Pablo JJ; Tirrell MV Phase Behavior and Salt Partitioning in Polyelectrolyte Complex Coacervates. Macromolecules 2018, 51, 2988–2995.

(46). Yim W; Zhou J; Sasi L; Zhao J; Yeung J; Cheng Y; Jin Z; Johnson W; Xu M; Palma-Chavez J; Fu L; Qi B; Retout M; Shah NJ; Bae J; Jokerst JV 3D-Bioprinted Phantom with Human Skin Phototypes for Biomedical Optics. Adv. Mater 2023, 35, 2206385.

(47). Armbruster DA; Pry T Limit of blank, limit of detection and limit of quantitation. Clin. Biochem. Rev 2008, 29, S49–S52. [PubMed: 18852857]

(48). Jin Z; Jorns A; Yim W; Wing R; Mantri Y; Zhou J; Zhou J; Wu Z; Moore C; Penny WF; Jokerst JV Mapping Aerosolized Saliva on Face Coverings for Biosensing Applications. Anal. Chem 2021, 93, 11025–11032. [PubMed: 34309356]

(49). Jin Z; Ling C; Li Y; Zhou J; Li K; Yim W; Yeung J; Chang Y-C; He T; Cheng Y; Fajtová P; Retout M; O'Donoghue AJ; Jokerst JV Spacer Matters: All-Peptide-Based Ligand for Promoting Interfacial Proteolysis and Plasmonic Coupling. Nano Lett. 2022, 22, 8932–8940. [PubMed: 36346642]

(50). Zhang L; Lin D; Sun X; Curth U; Drosten C; Sauerhering L; Becker S; Rox K; Hilgenfeld R Crystal structure of SARS-CoV-2 main protease provides a basis for design of improved ketoamide inhibitors. Science 2020, 368, 409–412. [PubMed: 32198291]

(51). Jin Z; Dridi N; Palui G; Palomo V; Jokerst JV; Dawson PE; Sang Q-XA; Mattoussi H Quantum Dot–Peptide Conjugates as Energy Transfer Probes for Sensing the Proteolytic Activity of Matrix Metalloproteinase-14. Anal. Chem 2023, 95, 2713–2722. [PubMed: 36705737]

(52). Jin Z; Dridi N; Palui G; Palomo V; Jokerst JV; Dawson PE; Amy Sang Q-X; Mattoussi H Evaluating the Catalytic Efficiency of the Human Membrane-type 1 Matrix Metalloproteinase (MMP-14) Using AuNP–Peptide Conjugates. J. Am. Chem. Soc 2023, 145, 4570–4582. [PubMed: 36802544]

(53). Algar WR; Malonoski A; Deschamps JR; Blanco-Canosa JB; Susumu K; Stewart MH; Johnson BJ; Dawson PE; Medintz IL Proteolytic Activity at Quantum Dot-Conjugates: Kinetic Analysis Reveals Enhanced Enzyme Activity and Localized Interfacial "Hopping. Nano Lett. 2012, 12, 3793–3802. [PubMed: 22731798]

(54). Henderson PJ A linear equation that describes the steady-state kinetics of enzymes and subcellular particles interacting with tightly bound inhibitors. Biochem. J 1972, 127, 321–333. [PubMed: 4263188]

(55). Hurst DR; Schwartz MA; Ghaffari MA; Jin Y; Tschesche H; Fields GB; Sang Q-XA Catalytic- and ecto-domains of membrane type 1-matrix metalloproteinase have similar inhibition profiles but distinct endopeptidase activities. Biochem. J 2004, 377, 775–779. [PubMed: 14533979]

(56). Lu J; Chen SA; Khan MB; Brassard R; Arutyunova E; Lamer T; Vuong W; Fischer C; Young HS; Vederas JC; Lemieux MJ Crystallization of Feline Coronavirus Mpro With GC376 Reveals Mechanism of Inhibition. Front. Chem 2022, 10, 852210. [PubMed: 35281564]

(57). Zhou J; Yim W; Zhou J; Jin Z; Xu M; Mantri Y; He T; Cheng Y; Fu L; Jokerst JV; et al. A fiber optic photoacoustic sensor for real-time heparin monitoring. Biosens. Bioelectron 2022, 196, 113692. [PubMed: 34653712] ;;

(58). Black KA; Priftis D; Perry SL; Yip J; Byun WY; Tirrell M Protein Encapsulation via Polypeptide Complex Coacervation. ACS Macro Lett. 2014, 3, 1088–1091. [PubMed: 35610798]

(59). Kaman WE; Galassi F; de Soet JJ; Bizzarro S; Loos BG; Veerman EC; van Belkum A; Hays JP; Bikker FJ Highly specific protease-based approach for detection of porphyromonas gingivalis in diagnosis of periodontitis. J. Clin. Microbiol 2012, 50, 104–12. [PubMed: 22075590]

(60). Moroz P; Jin Z; Sugiyama Y; Lara DA; Razgoniaeva N; Yang M; Kholmicheva N; Khon D; Mattoussi H; Zamkov M Competition of Charge and Energy Transfer Processes in Donor–Acceptor Fluorescence Pairs: Calibrating the Spectroscopic Ruler. ACS Nano 2018, 12, 5657–5665. [PubMed: 29883087]

(61). Shi H; Zhao N; Ding D; Liang J; Tang BZ; Liu B Fluorescent light-up probe with aggregation-induced emission characteristics for in vivo imaging of cell apoptosis. Org. Biomol. Chem 2013, 11, 7289–7296. [PubMed: 24077521]

(62). Yang S; Yu H; Xu X; Yang T; Wei Y; Zan R; Zhang X; Ma Q; Shum HC; Song Y AIEgen-Conjugated Phase-Separating Peptides Illuminate Intracellular RNA through Coacervation-Induced Emission. ACS Nano 2023, 17, 8195–8203. [PubMed: 37093110]

(63). Wu H; Qiao Y Engineering coacervate droplets towards the building of multiplex biomimetic protocells. Supramol. Chem 2022, 1, 100019.

(64). Mishra D; Wang S; Jin Z; Xin Y; Lochner E; Mattoussi H Highly fluorescent hybrid Au/Ag nanoclusters stabilized with poly(ethylene glycol)- and zwitterion-modified thiolate ligands. Phys. Chem. Chem. Phys 2019, 21, 21317–21328. [PubMed: 31531429]

(65). Fernandez A; Krishna J; Anson F; Dinsmore AD; Thayumanavan S Consequences of Noncovalent Interfacial Contacts between Nanoparticles and Giant Vesicles. Angew. Chem., Int. Ed 2022, 61, e202208616.

(66). Zhao P; Qu F; Fu H; Zhao J; Guo J; Xu J; Ho Y-P; Chan MK; Bian L Water-Immiscible Coacervate as a Liquid Magnetic Robot for Intravascular Navigation. J. Am. Chem. Soc 2023, 145, 3312–3317. [PubMed: 36728932]
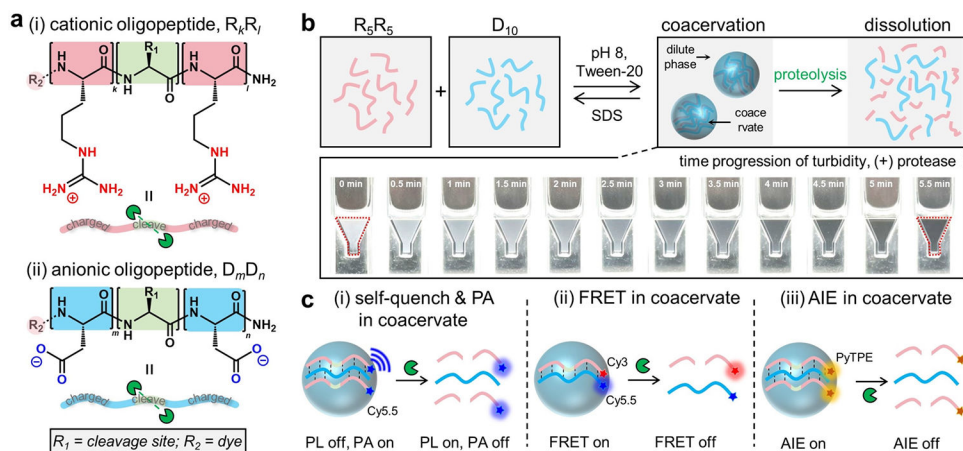
Figure 1.

Protease-responsive oligopeptide-based coacervates. (a) Complex coacervates comprise cationic Arg-rich and anionic Asp-rich oligopeptides. The substrates have a cleavage site (R_1) and a free N-terminal amine for dye conjugation (R_2). (b) A mixture of R_5R_5 and D_{10} at pH 8 results in a turbid emulsion containing the coacervates. Addition of M^{pro} leads to a clear solution. The electrostatic interactions holding the coacervates can be broken by SDS surfactant. (c) The confinement structure enables signal transductions in coacervates such as self-quenching, fluorescence resonance energy transfer (FRET), and aggregation-induced emission (AIE). After proteolysis, photoluminescence (PL) recovers in the FRET and self-quenching systems, whereas PL in the AIE system decreases.
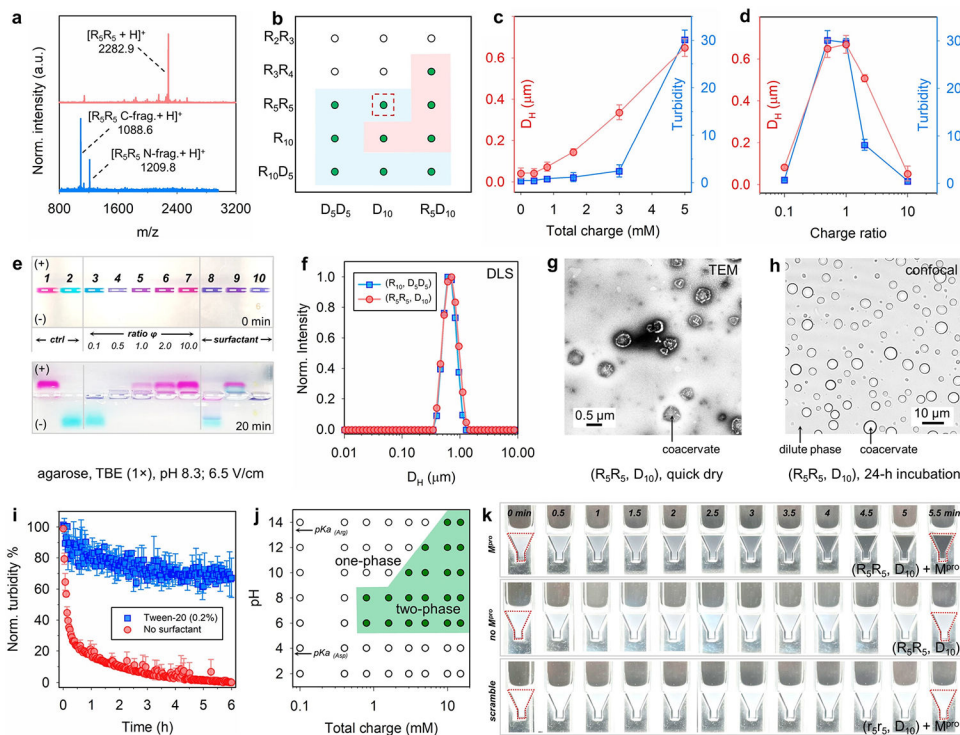
Figure 2.
Optimization of oligopeptide coacervation. (a) MALDI-TOF MS data show that M^{pro} cleaves the R_5R_5 substrate. The intact and fragments are shown in red and blue profiles, respectively. (b) Modular peptides of varying charge valence, charge density, and net charge are investigated for complex coacervation. The empty and green dots indicate no formation and the formation of coacervates, respectively. The blue and pink shadows designate relatively stable and unstable coacervates, respectively. Representative coacervates (R_5R_5, D_{10}) are highlighted in the dashed red box. (c) Increasing total charge increases the hydrodynamic diameter (D_H) and turbidity of freshly mixed coacervates. (d) The relation between the charge ratio (i.e., [Arg]/[Asp]) and D_H/turbidity of freshly mixed coacervates. (e) Agarose gel electrophoresis acquired from the fluorogenic (Cy3-R_5R_5, Cy5.5-D_{10}) coacervates of varying charge ratios (wells 3 to 7), side-by-side with the controls (Cy3-R_5R_5 and Cy5.5-D_{10} only in wells 1 to 2) and the coacervates with 0.2% surfactant (SDS, CTAB, and Tween-20 in wells 8 to 10). The optimal charge stoichiometry is 0.5 in well 4.[31] (f) DLS profiles of submicron coacervates by freshly mixing R_5R_5 with D_{10} (red) or R_{10} with D_5D_5 (blue). (g) TEM image of the negative-stained coacervates. (h) Bright-field confocal image of the coacervates aged for 24 h. The size is 3.0 ± 1.1 μm. (i) The turbidity decay of the (R_5R_5, D_{10}) coacervates with (blue) and without (red) 0.2% w/v Tween-20. (j) Phase diagram indicates that pH 6–8 is the optimal pH range for (R_5R_5, D_{10}) coacervation. The green area designates coacervation. (k) Time-dependent turbidity decay of the (R_5R_5, D_{10}) coacervates with M^{pro}. [S]/[E] = 800:1 was applied. Controls used were without M^{pro} and a scrambled r_5r_5 peptide with M^{pro}. The conditions used the R_5R_5 and D_{10} at 5.0 mM total charge, 0.5 charge ratio, pH 8, and 0.2% Tween-20, unless otherwise specified. Error bars = standard deviations ($n = 3$).
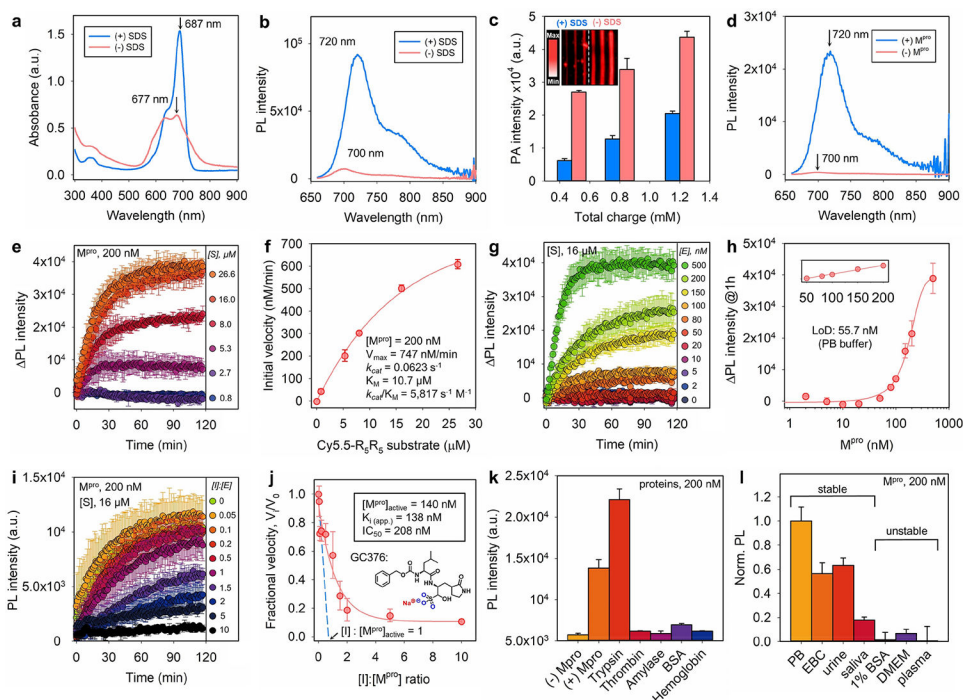
Figure 3.
Enzyme studies of the self-quenching-based (Cy5.5-R_5R_5, D_{10}) coacervates. Absorption (a) and PL (b) of the coacervates with (blue) and without (red) 1% SDS. (c) Photoacoustic (PA) performance of the coacervates with (blue) and without (red) SDS at total charges of 0.48, 0.8, and 1.2 mM. Inset shows the corresponding PA image. (d) The optical profiles of the coacervates with/without M^{pro}. (e) Time-dependent $PL_{720\,nm}$ of the coacervates at various total charges (0.024–0.8 mM) incubated with M^{pro} (200 nM). This corresponds to final [S] concentrations of 0.8–26.6 μM. (f) Determination of $k_{cat}/K_M = 5817$ M^{-1} s^{-1} for hydrolysis of the fluorogenic coacervates by M^{pro} in 20 mM PB, pH 8.0, at 37 °C. (g) Time progression of $PL_{720\,nm}$ in enzyme sensitivity assays, where the coacervates at 0.48 mM total charge ([S] = 16 μM) were incubated with increasing M^{pro} concentrations from 0–500 nM. (h) The $PL_{720\,nm}$ as a function of M^{pro} concentration was extracted from panel (g) at 1 h. The limit of detection (LoD) is 55.7 nM in PB buffer. The inset shows the linear fit for LoD calculation.[47] (i) Time-dependent $PL_{720\,nm}$ in inhibition assays. Increasing molar ratio of [I]/[E] from 0–10 was employed where GC376 is used as the inhibitor. (j) Inhibition curve collected by titrating M^{pro} (200 nM) with varying amounts of GC376; the coacervates at 0.48 mM total charge were used. The inset shows the chemical structure of GC376 inhibitor. (k) The reactivity of the fluorogenic coacervates toward other proteins (200 nM).[48] (l) The interactions of the fluorogenic coacervates with M^{pro} in biological matrices. All the above time progression data were collected every 1 min for 2 h, and $PL_{720\,nm} = PL_t - PL_0$ was used for the plot. Error bars = standard deviations ($n = 3$).
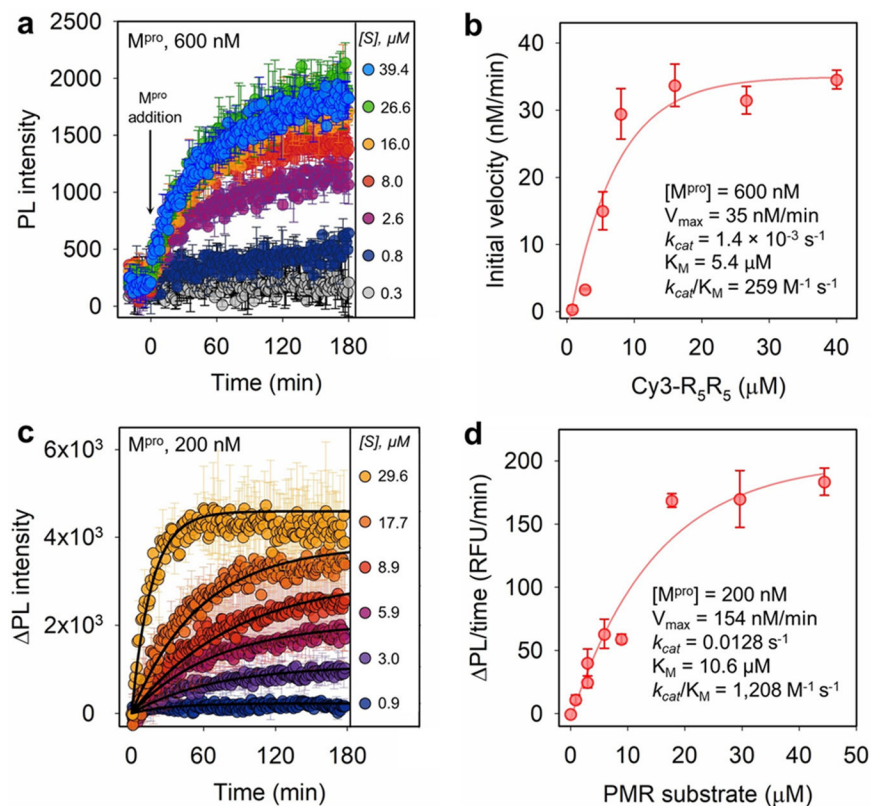
Figure 4.

Kinetic study using FRET-based (Cy3-R$_5$R$_5$, Cy5.5-D$_{10}$) and AIE-based (PMR, D$_{10}$) coacervates. (a) Time-dependent PL$_{560\ nm}$ recovery of the FRET coacervates at varying total charges from 0.024 to 1.2 mM incubated with M^{pro} (600 nM). This corresponds to final Cy3-R$_5$R$_5$ concentrations from 0.8 to 39.4 μM. (b) Determination of k_{cat}/K_M for the hydrolysis of the FRET coacervates by M^{pro}. (c) Time-dependent PL$_{550\ nm}$ recovery of the AIE coacervates at varying total charges (0.024–0.8 mM) incubated with M^{pro} (200 nM). This corresponds to final PMR concentrations from 0.9 to 29.6 μM. The inverse PL = PL$_0$ − PL$_t$ was used for the plot. Fits of PL versus t at each enzyme concentration using Eq. S7 are provided as solid black lines. (d) Determination of k_{cat}/K_M for hydrolysis of the AIE coacervates by M^{pro}. Error bars = standard deviations (n = 3).
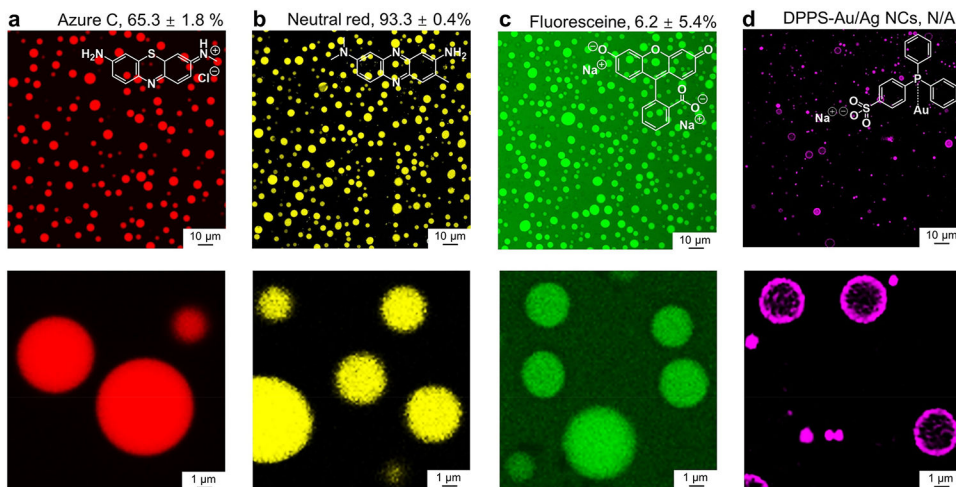
Figure 5.
Encapsulation of representative fluorescent materials in (R_5R_5, D_{10}) coacervates. Confocal images of coacervates sequestering (a) cationic azure A, (b) hydrophobic neutral red, (c) anionic fluorescein, and (d) anionic DPPS-coated Au/Ag nanoclusters. Inset shows the chemical structure. The value on top designates the encapsulation efficiency (EE%). A close look for each panel is provided in the second row. Confocal images of other encapsulants are listed in Figure S15.

Table 1.

Information on the (Dye-)Oligopeptides for Complex Coacervation

Effect	Peptide name	Peptide sequence[a]	M.W. [g/mol]	Net charge[b]	Description
charge valency, charge density	R_2R_3	RRAVLQ↓SGFRRR	1499.9	+5	cationic
	R_3R_4	RRRAVLQ↓SGFRRRR	1813.1	+7	cationic
	R_5R_5	RRRRRAVLQ↓SGFRRRRR	2280.4	+10	cationic
	r_5f_5	RRRRRQ × FAGSLVRRRRR	2280.4	+10	cationic, scramble
	R_{10}	RRRRRRRRRR	1578.0	+10	cationic
net charge	$R_{10}D_5$	RRRRRRRRRRRAVLQ↓SGFDDDDD	2855.5	+5	zwitterionic
	$R_{10}D_{10}$	RRRRRRRRRRRAVLQ↓SGFDDDDDDDDDD	3430.6	0	zwitterionic
	R_5D_{10}	RRRRRAVLQ↓SGFDDDDDDDDDD	2650.2	−5	zwitterionic
charge density	D_5D_5	DDDDDAVLQ↓SGFDDDDD	1869.6	−10	anionic
	D_{10}	DDDDDDDDDD	1167.3	−10	anionic
signal transductions	Cy5.5-R_5R_5	Cy5.5-RRRRRAVLQ↓SGFRRRRR	2850.7	+11	cationic, for self-quenching
	Cy3-R_5R_5	Cy3-RRRRRAVLQ↓SGFRRRRR	2721.4	+11	cationic, for FRET
	Cy5.5-D_{10}	Cy5.5-DDDDDDDDDD	1733.7	−9	anionic, for FRET and self-quenching
	PMR[28]	PyTPE-(Pra)GSAVLQ↓SGFRKMAGRRRRRR	2989.7	+9	cationic, for AIE
	PyTPE-R_5R_5	PyTPE-(Pra)GRRRRRAVLQ↓SGFRRRR[c]	2965.4	+11	cationic, for AIE
molecular probe	Cy5.5-R_5R_5-Cy3	Cy5.5-RRRRRAVLQ↓SGFRRRRRC-Cy3	3528.1	+12	FRET probe

[a] All peptides contain a free N-terminal amine and an amidated C-terminus; "↓" designates the M^{pro} cleavage site (coded in green); "×" designates noncleavable sequence by M^{pro}. NHS-ester dye was conjugated to the N-terminal amine.

[b] The electrophoretic property of peptide at pH 8.0, where the N-terminal amine is neutral in charge, and the dye (Cy and PyTPE) contributes to the net charge.[29,30]

[c] "Pra" designates propargylglycine.

Table 2.

Hydrodynamic Size (D_{H}), Polydispersity Index (PDI), and Surface Potential of the Representative Peptide Coacevates

Peptides	D_{H} (μm)	PDI	Zeta potential (mV)
(R_2R_3, D_{10})	N.D.[a]	N.D.	N.D.
(R_3R_4, D_{10})	N.D.	N.D.	N.D.
(R_5R_5, D_{10})	0.64	0.10	-6.2 ± 0.8
(R_{10}, D_5D_5)	0.68	0.02	-7.4 ± 1.7
$(R_{10}D_5, D_{10})$[b]	0.25	0.01	-10.4 ± 1.1
(R_{10}, R_5D_{10})[b]	1.30	0.05	$+4.4 \pm 0.5$
$(R_{10}D_{10})$[b]	1.78	0.05	$+5.7 \pm 0.3$

[a]·'N.D.' designates coacervate Not Detected by DLS. The conditions used 5 mM total charge, 0.5 charge ratio, 20 mM PB at pH 8, and 0.2% Tween-20 unless otherwise specified.

[b]For zwitterionic peptides, the charge ratio uses [Arg, (+)] = [net-positively charged peptide] × Arg valence, and [Asp, (−)] = [net-negatively charged peptide] × Asp valence. *Remark:* the charge ratio in $D_{10}R_{10}$ self-coacervates is 1.

Table 3.

Kinetic Parameters for M^{pro} Interacting with Fluorogenic Coacervates

Transduction mechanism	Component	M^{pro}, nM	v_{max}, nM/min	k_{cat}, s^{-1}	K$_M$, μM	k_{cat}/K_M, M^{-1} s^{-1}	Digestion yield[b]
FRET probe	Cy5.5-R$_5$R$_5$C-Cy3	200	780	0.065	12.6	5,159	85%
Self-quenching coacervate	(Cy5.5-R$_5$R$_5$, D$_{10}$)	200	747	0.062	10.7	5,817	75%
Self-quenching coacervate	(Cy5.5-R$_5$R$_5$, Cy5.5-D$_{10}$)	200	N.D.[a]	N.D.	N.D.	N.D.	0%
FRET coacervate	(Cy3-R$_5$R$_5$, Cy5.5-D$_{10}$)	600	35	0.0014	5.4	259	5%
AIE coacervates	(PMR, D$_{10}$)	200	154	0.013	10.6	1,208	N.D.

[a]'N.D.' designates Not Determined.

[b]The yield for FRET probe is from area integration in HPLC (Figure S10), and that for coacervates is estimated from the absorbance of the supernatant using εCy3 = 1.5 × 10^5 M^{-1} cm^{-1} at Abs555 nm and εCy5.5 = 1.98 × 10^5 M^{-1} cm^{-1} at Abs685 nm.

Table 4.

Coacervates in Encapsulation and Protease-Mediated Dye Release

Dye	Encapsulation efficiency, EE%	Partition coefficient, K	Release efficiency, RE%, by M^{pro}
Azure A	50 ± 1%	1.0	95 ± 1%
Azure C	65 ± 2%	1.9	98 ± 1%
MB	58 ± 2%	1.4	96 ± 1%
Rhodamine B	56 ± 1%	1.3	96 ± 2%
Rhodamine 6G	64 ± 4%	1.8	98 ± 1%
Neutral red	93 ± 1%	13.9	99 ± 1%
Fluoresceine	6 ± 5%	0.1	73 ± 7%